

Chapter 2

Coating Flows and Contact Line Models

2.1 Thin-Film Flow Down an Inclined Plane

2.1.1 Nondimensional Model Formulation

The model of gravity-driven flow formulated in Sect. 1.3 was based on the assumption that the inclined solid surface is initially covered with a liquid film. In experiments, the solid surface is often initially dry and is gradually covered by the liquid film as the leading edge of the film moves down under the action of gravity. Studies of this configuration are important for a number of applications involving coating of a solid surface with a layer of liquid (which is often solidified after the coating is complete). Even though in practical applications on the microscale, such as manufacturing computer hard drives, centrifugal force rather than gravity drives the flow, the key issues in mathematical modeling are essentially the same; we focus on the gravity-driven film flow in the present section.

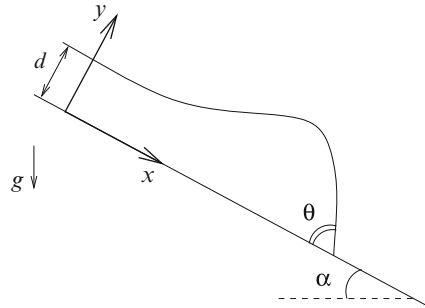
Consider a film of viscous liquid of density ρ and viscosity μ flowing down a plane inclined at an angle α , as illustrated in Fig. 2.1. As in Sect. 1.3, the flow is assumed to be two-dimensional, with no variations in the direction normal to the plane of the sketch. Far away from the leading edge the film is approximately flat and therefore the flow is described by the constant-thickness solution obtained in Sect. 1.3, with the average flow velocity $\rho g d^2 \sin \alpha / 3\mu$. It is convenient to define the characteristic flow velocity by:

$$U = \frac{\rho g d^2}{\mu} \sin \alpha \quad (2.1)$$

and the capillary number based on this velocity as:

$$\text{Ca} = \frac{\mu U}{\sigma}. \quad (2.2)$$

Fig. 2.1 Sketch of gravity-driven two-dimensional flow with a finite contact angle



Here, the surface tension σ is assumed constant. At the leading edge of the film, the liquid–gas interface is assumed to be meeting the solid surface at a contact angle θ , as shown in Fig. 2.1. The point of contact between the interfaces in the cross-sectional sketch in Fig. 2.1 corresponds to a line in the actual experiment; this line is moving downward and will be referred to as a *moving contact line*.

Let us now recall the lubrication-type model of a deforming film on a horizontal solid substrate formulated in Sect. 1.4. It was argued there that if the characteristic length scale in the horizontal direction is much larger than the film thickness, equations for liquid flow can be simplified to the system (1.46)–(1.48) or, in nondimensional form, to (1.56)–(1.58). The same arguments can be repeated for the present case of a film on an inclined surface if the length scale of change of film thickness along the plate is much larger than d , except that now gravity has a nonzero projection onto the x -direction, i.e., along the incline. Thus, instead of (1.56)–(1.58) we write (now using subscripts to denote derivatives)

$$p_x = u_{yy} + 1, \quad (2.3)$$

$$p_y = 0, \quad (2.4)$$

$$u_x + v_y = 0. \quad (2.5)$$

Here, x and y are the *nondimensional* Cartesian coordinates scaled by $d/\text{Ca}^{1/3}$ and d , respectively; u is the velocity component in the x -direction scaled by U , v is the velocity component in the y -direction scaled by $\text{Ca}^{1/3}U$, p is difference between the dimensional pressure and the atmospheric pressure scaled by $\text{Ca}^{2/3}\sigma/d$. In Chap. 1 we used tildas to distinguish nondimensional variables from the dimensional ones. In the present chapter, all variables will be assumed nondimensional unless noted otherwise and we will not use tildas. The component of gravity in the y -direction does not appear in our lubrication-type model although it can play an important role in experiments at small values of the inclination angle α . This motivated a slightly different set of assumptions about characteristic scales used, e.g., in Bertozzi and Brenner [17].

The scaled interfacial boundary conditions (1.61)–(1.62) formulated in Sect. 1.4 still apply (except that there is no temperature gradient along the interface) and are written in the notation of the present section as:

$$h_t + uh_x - v = 0 \quad \text{at} \quad y = h(x, t), \quad (2.6)$$

$$u_y = 0 \quad \text{at} \quad y = h(x, t), \quad (2.7)$$

$$p = -h_{xx} \quad \text{at} \quad y = h(x, t), \quad (2.8)$$

where the interface location is described by the function $y = h(x, t)$ and t is nondimensional time, scaled by $\text{Ca}^{-1/3}d/U$.

At the solid boundary, the no-slip condition is satisfied and the normal velocity is zero, so

$$u = 0 \quad \text{at} \quad y = 0, \quad (2.9)$$

$$v = 0 \quad \text{at} \quad y = 0. \quad (2.10)$$

By repeating the same steps as in the derivation of (1.66) in Sect. 1.4, (2.5), (2.6), and (2.10) yield

$$h_t + \left(\int_0^h u dy \right)_x = 0. \quad (2.11)$$

Since according to (2.4), p is a function of x and t only, (2.3) can be integrated twice in y to give the following velocity profile,

$$u = \frac{1}{2}(p_x - 1)(y^2 - 2yh). \quad (2.12)$$

Here, we used (2.7) and (2.9) to determine the two constants of integration. By taking into account the boundary condition (2.8), we find

$$u = -\frac{1}{2}(h_{xx} + 1)(y^2 - 2yh). \quad (2.13)$$

By substituting this velocity profile into (2.11) we obtain an evolution equation for the interface shape in the form

$$h_t + \frac{1}{3}(h^3 h_{xx})_x + h^2 h_x = 0. \quad (2.14)$$

The lubrication-type approach resulting in this equation is applicable to the situation sketched in Fig 2.1 only when the contact angle θ is sufficiently small. In fact, since the contact angle is the inverse tangent of the absolute value of the interface slope at the contact line, the value of θ has to be of the same order of magnitude as $\text{Ca}^{1/3}$, as discussed in more detail in Goodwin and Homsy [58]. From now on, we use the re-scaled contact angle Θ defined by $\Theta = \theta \text{Ca}^{-1/3}$. We assume that Θ is a constant independent of the contact line speed or any other quantities related to the flow and impose the boundary condition

$$h_x(x_{\text{CL}}, t) = -\Theta, \quad (2.15)$$

where $x_{\text{CL}} = x_{\text{CL}}(t)$ is the contact-line location which has to be determined as part of the solution in such a way that the condition (2.15) is satisfied and

$$h(x_{\text{CL}}, t) = 0. \quad (2.16)$$

Assuming that the film is flat near $x = 0$, the boundary conditions there are

$$h = 1, \quad h_x = 0 \quad \text{at} \quad x = 0. \quad (2.17)$$

The initial condition needed to complete the model formulation is not easy to specify because it depends on the particular choice of the starting procedure in experiments. Fortunately, some results, which turn out to be very important for practical applications, can be obtained using a simplified framework, in which the shape of the interface is assumed stationary (i.e., not changing in time) in a reference frame moving downward with the contact line, at a speed u_{CL} . In this reference frame, the interface is described by a function $h_0(\hat{x})$, $\hat{x} = x - u_{\text{CL}}t$ and the substrate is moving with the velocity $-u_{\text{CL}}$. The boundary condition (2.9) is then replaced with

$$u = -u_{\text{CL}} \quad \text{at} \quad y = 0. \quad (2.18)$$

Near $\hat{x} = 0$, the film is flat and of unit thickness, so the velocity profile satisfying the condition (2.18) together with $u_y = 0$ at the interface is

$$u = -\frac{1}{2}(y^2 - 2y) - u_{\text{CL}}. \quad (2.19)$$

The integral of this profile from 0 to 1 has to be zero since otherwise the amount of liquid between $\hat{x} = 0$ and the contact line would change and the interface would not remain stationary. Integrating (2.19) gives the condition $u_{\text{CL}} = \frac{1}{3}$, simply reflecting the fact that the contact line speed is equal to the average flow velocity. Now, by using $\hat{x} = x - t/3$ and the chain rule, (2.14) is simplified to an ordinary differential equation in \hat{x} :

$$-\frac{1}{3}h'_0 + \frac{1}{3}(h_0^3 h_0''')' + h_0^2 h'_0 = 0, \quad (2.20)$$

where primes are used to denote differentiation with respect to \hat{x} . This equation can be integrated once, resulting in

$$h_0^2 h_0''' = 1 - h_0^2. \quad (2.21)$$

The constant of integration is set to zero based on the condition that in the flat part of the film ($h_0''' = 0$) the value of h_0 is equal to unity.

Equation (2.21) has to be solved on the domain $[0, \hat{x}_{\text{CL}}]$ with the contact line coordinate \hat{x}_{CL} chosen large enough to ensure that the liquid film is flat near $\hat{x} = 0$. We choose $\hat{x}_{\text{CL}} = 10$ and use the boundary conditions

$$h'_0(0) = 0, \quad h_0(\hat{x}_{\text{CL}}) = 0, \quad h'_0(\hat{x}_{\text{CL}}) = -\Theta. \quad (2.22)$$

2.1.2 Shear-Stress Singularity

It may seem that the interface shape can now be easily found by solving the boundary value problem defined by (2.21) and (2.22). However, severe convergence problems are encountered if one tries to solve this system numerically, e.g., using the `bvp4c` solver from MATLAB. To understand the origin of the numerical difficulties let us analyze (2.21) for values of \hat{x} approaching \hat{x}_{CL} . First, we note that since $h_0 \rightarrow 0$ as $\hat{x} \rightarrow \hat{x}_{\text{CL}}$, (2.21) requires that $h_0''' \rightarrow \infty$ near the contact line. Clearly, a solution with this property cannot be accurately described by the standard numerical methods which rely on the assumption that all derivatives of the solution are bounded. Even though some advanced numerical methods can handle situations when the derivatives are unbounded, we will not attempt to solve the boundary value problem defined by (2.21) and (2.22) numerically because solutions with $h_0''' \rightarrow \infty$ at the contact line are not physically meaningful: predictions based on such a solution are in obvious contradiction with physical reality. To illustrate this point, let us calculate the shear-stress at the solid–liquid interface based on such a solution. Based on (2.13),

$$u_y|_{y=0} = h(h_{\text{xxx}} + 1), \quad (2.23)$$

or, in the moving reference frame,

$$u_y|_{y=0} = h_0(h_0''' + 1). \quad (2.24)$$

Using (2.21), this equation can be written as:

$$u_y|_{y=0} = h_0^{-1}. \quad (2.25)$$

The right-hand side of this equation clearly goes to infinity as $h_0 \rightarrow 0$, so the shear-stress is singular at the contact line. The total tangential force acting at the solid–liquid boundary between a point \hat{x} and the contact line is determined by integrating the shear-stress over the area of contact and is proportional to the nondimensional quantity

$$f \equiv \int_{\hat{x}}^{\hat{x}_{\text{CL}}} u_y|_{y=0} ds = \lim_{\hat{X} \rightarrow \hat{x}_{\text{CL}}^-} \int_{\hat{x}}^{\hat{X}} h_0^{-1} ds. \quad (2.26)$$

Here we used (2.25) and the standard definition of an improper integral. If the point \hat{x} is sufficiently close to the contact line, we can approximate local interface shape by a linear function, i.e.,

$$h_0(s) = -\Theta(s - \hat{x}_{\text{CL}}), \quad \hat{x} \leq s \leq \hat{x}_{\text{CL}}. \quad (2.27)$$

By substituting this into the formula expressing f as a limit, (2.26), we obtain

$$f = - \lim_{\hat{x} \rightarrow \hat{x}_{\text{CL}}^-} \int_{\hat{x}}^{\hat{X}} \frac{ds}{\Theta(s - \hat{x}_{\text{CL}})} = - \lim_{\hat{X} \rightarrow \hat{x}_{\text{CL}}^-} \frac{1}{\Theta} \ln(\hat{x}_{\text{CL}} - \hat{X}) + \frac{1}{\Theta} \ln(\hat{x}_{\text{CL}} - \hat{x}) = \infty. \quad (2.28)$$

Thus, our solution predicts an *infinite* value of f , which implies that an infinite force is needed to move the film down an inclined surface, i.e., the film should not move. To provide an even more dramatic illustration of the nonphysical nature of the solution with the shear-stress singularity, consider the following situation. When a small solid object is floating in water, everyday experience suggests that a slight downward push is sufficient to completely immerse it into water. However, if the shear-stress at the moving contact line (where the solid touches the liquid surface) is indeed singular as described above, the resistance to downward motion should be infinite! As Huh and Scriven [68] put it, “not even Herakles could sink a solid if the physical model were entirely valid, which it is not.”

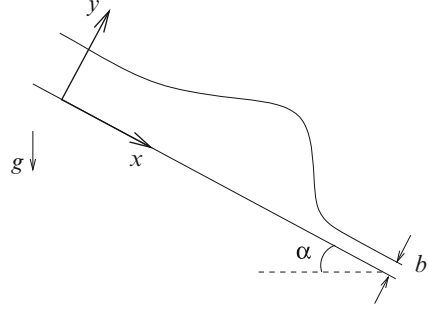
While the shear-stress singularity is illustrated here in the context of a simple coating flow, it turns out to be an intrinsic property of moving contact lines, not specific to the particular geometric configuration or to the use of the lubrication theory, as will become evident below in Sect. 2.1.7.

2.1.3 Removing the Singularity

Since the mathematical model developed in Sect. 2.1.1 leads to nonphysical predictions, it is natural to ask how to modify the model so that the physics of the viscous gravity-driven flow down an inclined plane is captured correctly. One such modification, which is particularly easy to implement in our framework, is based on the following experimental observation. When a liquid–gas interface appears to be in contact with the solid, careful experimental studies of the contact line region often indicate that the true contact is not really achieved. Instead, what appears to be dry solid is covered with a very thin film called a *precursor film* [55]. In other words, instead of the true contact between liquid, solid, and gas, as shown in Fig. 2.1, one may be dealing with a situation sketched in Fig. 2.2 (the scaled precursor film thickness b is exaggerated to improve the clarity of the picture).

While moving contact line in the model of Fig. 2.1 is defined precisely by the point at which the film thickness is zero, in the modified model one usually speaks of an *apparent* contact line, defined as a narrow transition region between the thicker film and much thinner precursor. The liquid–gas interface appears to be in contact with the solid there based on observations which do not resolve the precursor film. In some studies, the apparent contact line is defined more precisely by the location at which the interface curvature reaches its local maximum. Assuming that the apparent contact line is moving downward at a constant speed u_{CL} , we consider the moving reference frame such that $\hat{x} = x - u_{\text{CL}}t$ and \hat{x} is in the domain $[0, L]$. We

Fig. 2.2 Sketch of gravity-driven flow with a precursor film ahead of the apparent contact line. Precursor thickness is exaggerated for clarity



choose L large enough to ensure that the film is flat *both* near $\hat{x} = 0$ and near $\hat{x} = L$; the film thickness near $\hat{x} = L$ is equal to b . The velocity profile near the left endpoint of the domain is still given by (2.19), so the integral of the flow velocity across the film is

$$\int_0^1 u dy = \frac{1}{3} - u_{CL}. \quad (2.29)$$

In contrast to the case of true contact line, liquid is now entering the domain at the right endpoint. The velocity profile there is

$$u = -\frac{1}{2}(y^2 - 2yb) - u_{CL}. \quad (2.30)$$

If the interface, described by $h_0(\hat{x})$, is stationary in our moving reference frame, the total amount of liquid in the domain does not change and the integral of this profile from 0 to b should be equal to (2.29). This condition determines the value of the apparent contact line velocity,

$$u_{CL} = \frac{1 - b^3}{3(1 - b)}. \quad (2.31)$$

Substituting $h = h_0(x - u_{CL}t)$ into the evolution equation (2.14) and using primes to denote derivatives with respect to \hat{x} , we obtain

$$-u_{CL}h_0' + \frac{1}{3}(h_0^3 h_0''')' + h_0^2 h_0' = 0. \quad (2.32)$$

Integration in \hat{x} with the condition of flat film of unit thickness at $\hat{x} = 0$ leads to

$$h_0^2(h_0''' + 1) = 1 + b + b^2 - \frac{b(1+b)}{h_0}. \quad (2.33)$$

The thickness values are specified at the endpoints,

$$h_0(0) = 1, \quad h_0(L) = b, \quad (2.34)$$

and *all* derivatives have to be zero at both endpoints to ensure that the film is flat there. Clearly, this implies looking for a solution of a third-order equation (2.33) with more than three boundary conditions, so there is no a priori guarantee that such a solution exists. However, careful numerical studies indicate that for sufficiently large computational domain length L the appropriate solution can always be found.

2.1.4 Numerical Methods

The nonlinear boundary value problem formulated in the end of Sect. 2.1.3 can in principle be solved by discretizing the domain $[0, L]$, e.g., in a manner similar to Sect. 1.6, and using the finite-difference approximation of the third derivative to obtain a system of equations for the values of $h_0(\hat{x})$ at the mesh points. The classical Newton's method can then be used to solve the resulting nonlinear system iteratively, as described, e.g., in Kelley [75]. MATLAB codes suitable for iterative solutions of nonlinear systems of equations are available online (see [75] for details). However, these codes often fail to converge for the present problem with uniform mesh discretization. Numerical methods based on nonuniform mesh discretizations can have better convergence properties but they can also fail unless the initial condition is sufficiently close to the final solution. Obtaining such an accurate initial guess of the unknown solution is a challenging task. In recent years, the so-called pseudo-transient continuation methods have been gaining popularity for situations when the Newton's method and its variations have severe convergence problems [34]. The idea is to consider an unsteady extension of the steady state equations and use the method of lines, introduced in Sect. 1.6, to solve the unsteady problem until the solution reaches the steady state within a specified accuracy. Application of this idea to the present situation is especially straightforward since a transient version of (2.33) is readily available in the form of the original evolution equation for the interface shape, (2.14). A traveling-wave solutions of the latter equation was found by relatively minor modifications of the numerical method described in detail in Sect. 1.6. The corresponding MATLAB code can be found in Sect. B.2.1. The numerical method turns out to be quite robust and converges quickly even with the discontinuous initial condition of the form

$$h(\hat{x}, 0) = \begin{cases} 1, & 0 \leq \hat{x} \leq L/2, \\ b, & L/2 < \hat{x} \leq L. \end{cases} \quad (2.35)$$

An alternative approach to solving the boundary value problem from Sect. 2.1.3 is a shooting method developed by Tuck and Schwartz [131]. They use analytical results describing the local behavior of the solution to formulate the boundary

conditions at the left endpoint of the computational domain. To illustrate this approach, let us write the solution near $\hat{x} = 0$ in the form

$$h_0(\hat{x}) = 1 + a\zeta(\hat{x}), \quad (2.36)$$

where a is a small parameter and the unknown function ζ can be found by substituting (2.36) into (2.33) and linearizing in a (i.e., neglecting all terms which are nonlinear in a). The equation for ζ obtained by the linearization procedure is

$$\zeta''' + (2 - b - b^2)\zeta = 0. \quad (2.37)$$

Since $b < 1$, the solution of this linear ordinary differential equation which decays to zero at $-\infty$ can be written in the form

$$\zeta = e^{q\hat{x}} \cos(q\sqrt{3}\hat{x}), \quad (2.38)$$

where $q = (2 - b - b^2)^{1/3}/2$. The complementary solution involving sine instead of cosine can be eliminated by a shift in the origin of coordinates. By calculating the derivatives of ζ from (2.38) and evaluating the results at $\hat{x} = 0$, we obtain the following boundary conditions at the left endpoint of the computational domain for small a :

$$h_0(0) = 1 + a, \quad h'_0(0) = aq, \quad h''_0(0) = -2aq^2. \quad (2.39)$$

An even more accurate approximation to the solution near $\hat{x} = 0$ can be obtained by incorporating the corrections which are second order in the small parameter a , as was done in [131].

The boundary value problem for the interface shape based on (2.33) can be reformulated in terms of new functions $y_1 = h_0$, $y_2 = h'_0$, and $y_3 = h''_0$, as follows,

$$y'_1 = y_2, \quad (2.40)$$

$$y'_2 = y_3, \quad (2.41)$$

$$y'_3 = \frac{1 + b + b^2}{y_1^2} - \frac{b(1 + b)}{y_1^3} - 1, \quad (2.42)$$

$$y_1(0) = 1 + a, \quad y_2(0) = aq, \quad y_3(0) = -2aq^2, \quad y_1(L) = b. \quad (2.43)$$

The problem can now be solved (with a being a parameter varied as part of the shooting procedure) using standard numerical methods for first-order boundary value problems, e.g., the Matlab solver `bvp4c`. In practice, the terms which are second-order in a are incorporated in the numerical procedure. The MATLAB code for this method can be found in Sect. B.2.2. More details on using MATLAB solvers for boundary value problems can be found, e.g., in Chap. 3 of [110].

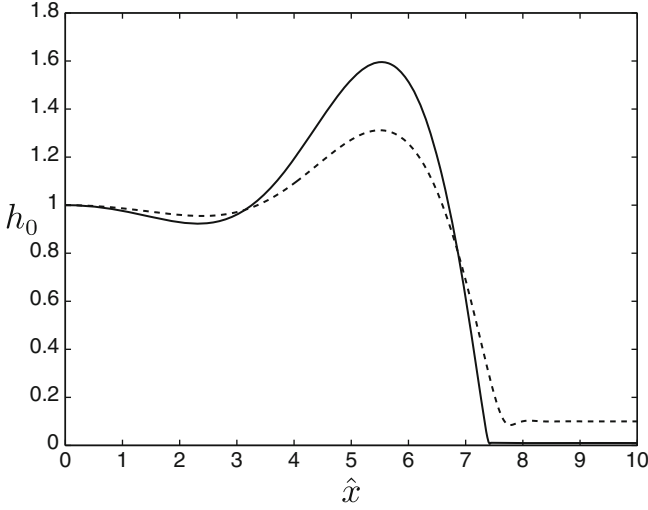


Fig. 2.3 Steady interface shapes in the moving reference frames for $b = 0.01$ (solid line) and $b = 0.1$ (dashed line)

2.1.5 Interface Shapes

Numerical results for interface shapes $h_0(\hat{x})$ are plotted in Fig. 2.3 for two different values of the scaled precursor thickness, b . The choice of the horizontal coordinate, $\hat{x} = x - u_{\text{CL}}t$, implies that the interface shapes in the plot are steady (i.e., independent of time). In terms of the original scaled variables, x and t , these results correspond to traveling wave solutions moving at a speed u_{CL} defined by (2.31). It is clear in Fig. 2.3 that liquid tends to accumulate behind the apparent contact line, forming a bump which is sometimes called the “capillary ridge.” By examining the dashed line we also observe that the minimum film thickness is slightly below b but clearly above zero. The same conclusion can be reached for the solid line if one zooms into the apparent contact line region. These observations can be used to clarify why the singularities in the shear-stress and the total resistance force are removed when the precursor film is introduced into the mathematical model. Recall that singularities in integrals such as the one in (2.28) appear only when the film thickness approaches zero and are clearly avoided when the thickness is above a positive number, even if that number is small.

The dimensional precursor film thickness is small compared to the length scale d , but is still assumed to be sufficiently large for the continuum approximation, introduced in Sect. 1.1, to be valid and for the disjoining pressure effects, discussed in Sect. 1.7, to be negligible. It turns out that even when the disjoining pressure defined by (1.129) is incorporated into the model, it does not affect the interface shapes away from the apparent contact line as long as the value of d is above $\sim 1 \mu\text{m}$.

The capillary ridge in Fig. 2.3 is higher for the smaller precursor thickness, but the difference in height is not dramatic despite the order of magnitude difference between the values of b . Let us investigate how the global interface shape depends on the precursor film thickness. In the region where h_0 approaches b , the natural length scale is defined by bd instead of the usual value of d , so (2.33) can be written in terms of new variables $H = h_0/b$ and $X = (\hat{x}_1 - \hat{x})/b$ (\hat{x}_1 being an arbitrary point in the apparent contact line region). The result, after neglecting several terms which are small in the limit of small b , is written as follows,

$$H^2 H''' = \frac{1}{H} - 1. \quad (2.44)$$

Here, we use primes to denote derivatives with respect to X . The interface shape at $h_0 \sim 1$ depends on the behavior of the solutions of (2.44) *outside* the contact line region, i.e., in the limit of $X \rightarrow \infty$. A solution which grows as X^2 in this limit can be obtained in the form of an infinite series [14], but it is clearly not applicable to our problem because it predicts a very large curvature away from the apparent contact line region. Thus, we follow Bender and Orszag [14] and look for a different asymptotic behavior of the solution at $X \rightarrow \infty$, of the form

$$H \sim AX(\ln X)^\beta. \quad (2.45)$$

By substituting this into (2.44), we find $\beta = 1/3$ and $A = 3^{1/3}$. The slope of the interface at large X can then be estimated from the formula

$$H_X = (3 \ln X)^{1/3}. \quad (2.46)$$

In terms of the variables h_0 and \hat{x} , this implies

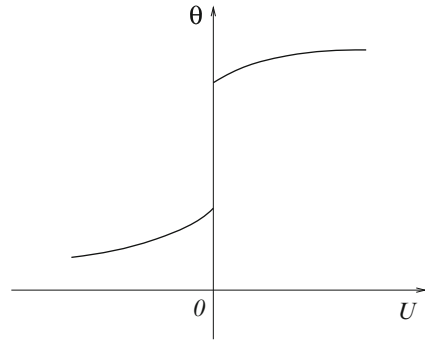
$$h'_0(\hat{x}) = - \left(3 \ln \frac{\hat{x}_1 - \hat{x}}{b} \right)^{1/3}. \quad (2.47)$$

In experiments, the apparent contact angle θ_{app} is typically determined as the absolute value of the slope angle measured at a dimensional distance l^* from the precursor film region, where l^*/d is much larger than b but small compared to $\text{Ca}^{-1/3}$. Based on (2.47) and the definitions of the length scales in the direction along the solid surface and normal to it ($d \text{Ca}^{-1/3}$ and d , respectively), we obtain

$$\theta_{\text{app}} = \text{Ca}^{1/3} \left(3 \ln \frac{l^* \text{Ca}^{1/3}}{bd} \right)^{1/3}. \quad (2.48)$$

Since the influence of the factor of $\text{Ca}^{1/3}$ in the logarithmic term on the value of θ_{app} is not very strong, although important for interpreting some experimental data [50],

Fig. 2.4 A sketch of dynamic contact angle versus velocity based on experimental data (after [70])



an approximate dependence of θ_{app} on the capillary number is often used instead of (2.48), in the form

$$\theta_{\text{app}} \sim \text{Ca}^{1/3}. \quad (2.49)$$

For comparison with experimental data, it is useful to note that the dimensional contact line speed, U_{CL} , in our model is approximately $U/3$, so (2.48) and (2.49) can be written as:

$$\theta_{\text{app}}^3 = \frac{9\mu U_{\text{CL}}}{\sigma} \ln \frac{l^*(3\mu U_{\text{CL}})^{1/3}}{\sigma^{1/3}bd} \quad (2.50)$$

and

$$\theta_{\text{app}}^3 \sim \frac{\mu U_{\text{CL}}}{\sigma}. \quad (2.51)$$

Most experimental data for the case of complete wetting is described by the approximate formula, (2.51), reasonably well. For the case when the static contact angle is nonzero, a more general equation, often called Tanner's law, has been used to describe dynamic contact angle data:

$$\theta^3 = \theta_0^3 + c_T \frac{\mu U_{\text{CL}}}{\sigma}, \quad (2.52)$$

where θ_0 is the static contact angle discussed in Chap. 1, c_T is an empirical constant close to 72. Equation (2.52) is also sometimes referred to as the Hoffman–Voinov–Tanner law or Cox–Voinov law to recognize the authors of the pioneering studies of dynamic contact angles [39, 66, 128, 134]. Finally, one feature of the experimental data not captured by either the precursor film model or the Tanner's law, is that the contact line can remain stationary for a range of contact angles. Thus, the actual experimental measurements often result in curves of the type sketched in Fig. 2.4. The negative velocity corresponds to the case of a receding contact line (discussed in more detail in Sect. 2.2).

While introduction of the precursor film into the model clearly allows one to remove the shear-stress singularity, strictly speaking it is only justified when such film is indeed present. Experiments indicate that this is not always the case and is in

fact unlikely when the observed value of the contact angle is not small. It is natural to ask how the singularity is removed when no precursor film is present. To answer this question, several studies use the notion of slip at the solid surface, introduced in Sect. 1.5*. However, instead of the simple model discussed there, they employ the so-called Navier–Greenspan model of slip, usually written in the form

$$u = \frac{\bar{\alpha}}{3h} \frac{\partial u}{\partial y} \quad \text{at} \quad y = 0, \quad (2.53)$$

where $\bar{\alpha}$ is a constant. The shear-stress singularity is avoided when this condition is used instead of the classical no-slip condition [59]. The value of the contact angle can then be specified in the simulation either as a constant equal to its static value, or as a known function of local velocity, e.g., based on an empirical formula, such as, (2.52) or an experimental curve. Remarkably, the interface shapes away from the contact line region for gravity-driven flow obtained using the Navier–Greenspan model and no precursor film are the same as with the precursor and no slip, as long as $\bar{\alpha} = b$ and both are sufficiently small [119].

An alternative approach to removing the shear-stress singularity has been proposed by Shikhmurzaev and described in detail in [111]. It does not require introduction of either precursor film or slip but rather uses the fact that surface tension is a dynamic quantity which cannot always be assumed equal to its value measured in static configurations. In particular, when an interface is created, the surface tension is initially different from the static value, but relaxes to it over some characteristic time τ_{rel} . Taking this effect into account results in singularity-free models of moving contact lines. However, the approach of Shikhmurzaev remains controversial. Its critics often point out that τ_{rel} used in his model are significantly higher than physically realistic values. More discussion of the issue of the characteristic relaxation times for surface tension can be found in [49, 112].

2.1.6 Stokes Flow: Equations for Stream Function and Vorticity

The models of gravity-driven flow discussed so far have an important limitation: they all are based on the assumption that the characteristic length scale in the direction along the incline is large compared to the film thickness. In experiments, this assumption is violated when films flow over a dry substrate (no precursor) and the contact angle θ (shown in Fig. 2.1) is not small. The Reynolds number $\text{Re} = Udp/\mu$ in many such experiments is still rather small, so the nonlinear terms in the Navier–Stokes equations can be neglected, resulting in the Stokes flow equations introduced in Sect. 1.5*. For the geometric configuration illustrated in Fig. 2.1, these equations can be formulated in nondimensional terms as:

$$p_x = \text{Ca}(\nabla^2 u + 1), \quad (2.54)$$

$$p_y = \text{Ca}(\nabla^2 v - \cot \alpha), \quad (2.55)$$

$$u_x + v_y = 0. \quad (2.56)$$

Here, $\nabla^2 = \partial_x^2 + \partial_y^2$, all length variables are scaled by d , the velocity components are scaled by U , and pressure is scaled by σ/d . These equations have to be solved with the no-penetration and the Navier–Greenspan slip condition (to avoid shear-stress singularity) at the solid wall and the general interfacial boundary conditions formulated in Sect. 1.5*. For the two-dimensional case considered here, it is often convenient to reformulate the problem in terms of the stream function ψ , defined by:

$$u = \psi_y, \quad v = -\psi_x. \quad (2.57)$$

The continuity equation (2.56) is now satisfied automatically. By differentiating equation (2.55) with respect to x and subtracting it from the y -derivative of (2.54), we obtain

$$\nabla^4 \psi = 0. \quad (2.58)$$

Here, we expressed the velocity components in terms of the stream function. For the purposes of numerical implementation, it is usually more convenient to use an equivalent system of partial differential equations,

$$\nabla^2 \psi = -\omega, \quad (2.59)$$

$$\nabla^2 \omega = 0, \quad (2.60)$$

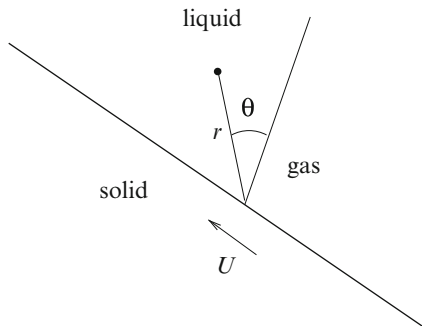
where $\omega = v_x - u_y$ is the vorticity component in the direction normal to the x – y plane (although in some numerical studies ω denotes the quantity $u_y - v_x$). Note that the derivations of (2.58) and (2.59)–(2.60) did not depend on the details of flow geometry, so these equations can be used for a wide range of different flows as long as the Reynolds numbers are small.

There is extensive literature on numerical methods for solving the Stokes flow equations. The details of these methods are beyond the scope of this book. For the geometric configuration shown in Fig. 2.1, numerical steady-state solutions of the Stokes flow equations with the Navier–Greenspan slip condition have been obtained by Goodwin and Homsy [58] using the boundary-element method. Comparison between their numerical results and the lubrication-type approach indicates that the latter works surprisingly well even for relatively large contact angles.

2.1.7 Local Flow Near Moving Contact Line

The shear-stress singularity has been discussed so far only in the context of a simplified model of gravity-driven flow, based on a lubrication-type approach. It is natural to wonder if the singularity may disappear if the characteristic lengths in the x - and y -directions are the same, denoted by d . To illustrate that this is not

Fig. 2.5 Sketch of local geometry and polar coordinates near a moving contact line



the case and to show that the shear-stress singularity is present in a wide range of different flows, let us consider local behavior of solutions of fluid flow equations in the vicinity of a contact line. Even if the flow domain has complicated geometry, near the contact line the geometry is that of a wedge formed by the liquid–gas and solid–liquid interfaces, as sketched in Fig. 2.5. It is therefore convenient to write the Stokes flow equations in terms of polar coordinates (r, θ) shown in the sketch (r is nondimensional, scaled by d). The value of the contact angle is denoted by $\hat{\theta}$ here. The radial and angular components of flow velocity, both scaled by a characteristic flow velocity U , can be expressed in terms of the stream function ψ in polar coordinates:

$$u_r = \frac{1}{r} \frac{\partial \psi}{\partial \theta}, \quad u_\theta = -\frac{\partial \psi}{\partial r}. \quad (2.61)$$

Assuming the Reynolds number, $\text{Re} = U d \rho / \mu$ is small, the Stokes flow approximation discussed in the previous subsection can be used. Using the well-known expression for ∇^2 in polar coordinates (see, e.g., Sect. A.6 in the Appendix of [1]), the Stokes flow equations in terms of the stream function and vorticity, (2.59) and (2.60), are written as:

$$\frac{1}{r} \frac{\partial}{\partial r} \left(r \frac{\partial \psi}{\partial r} \right) + \frac{1}{r^2} \frac{\partial^2 \psi}{\partial \theta^2} = -\omega, \quad (2.62)$$

$$\frac{1}{r} \frac{\partial}{\partial r} \left(r \frac{\partial \omega}{\partial r} \right) + \frac{1}{r^2} \frac{\partial^2 \omega}{\partial \theta^2} = 0. \quad (2.63)$$

Both ω and ψ are expected to be finite as $r \rightarrow 0$ (otherwise, the velocity components would be infinite, which is clearly nonphysical) and represented by a Taylor series near $r = 0$. In polar coordinates, this implies local behaviors in the form

$$\psi = r f_1(\theta) + O(r^2), \quad (2.64)$$

$$\omega = r f_2(\theta) + O(r^2), \quad (2.65)$$

where f_1 and f_2 are functions to be determined. In the limit of $r \rightarrow 0$, $O(r^m)$ here and below denotes any function $f(r, \theta)$ such that

$$\lim_{r \rightarrow 0} \frac{f(r, \theta)}{r^m} \quad (2.66)$$

exists for all θ between zero and $\hat{\theta}$.

By substituting (2.64) and (2.65) into (2.62) and (2.63), we obtain ordinary differential equations for f_1 and f_2 ,

$$f_1'' + f_1 = -f_2, \quad (2.67)$$

$$f_2'' + f_2 = 0, \quad (2.68)$$

and thus

$$f_1 = A \sin \theta + B \cos \theta + C \theta \sin \theta + D \theta \cos \theta. \quad (2.69)$$

The constants A , B , C , and D are found from the boundary conditions of zero normal velocity and zero tangential stress at the liquid–gas interface,

$$\frac{\partial \psi}{\partial r}(r, 0) = 0, \quad \frac{\partial^2 \psi}{\partial \theta^2}(r, 0) = 0, \quad (2.70)$$

and the conditions of zero normal and specified tangential velocity at the moving (in the reference frame of the contact line) solid wall,

$$\frac{\partial \psi}{\partial r}(r, \hat{\theta}) = 0, \quad -\frac{1}{r} \frac{\partial \psi}{\partial \theta}(r, \hat{\theta}) = u_{\text{CL}}. \quad (2.71)$$

From the conditions at the liquid–gas interface (2.70), we immediately obtain $B = 0$ and $C = 0$. The remaining two conditions (2.71) result in a linear system of algebraic equations for the coefficients A and D . By solving this system, we obtain

$$A = u_{\text{CL}} \left(\frac{\sin \hat{\theta}}{\hat{\theta}} - \frac{1}{\cos \hat{\theta}} \right)^{-1}, \quad (2.72)$$

$$D = u_{\text{CL}} \left(\frac{\hat{\theta}}{\sin \hat{\theta}} - \cos \hat{\theta} \right)^{-1}. \quad (2.73)$$

Thus, all unknown constants have been found and therefore the behavior of the components of the stress tensor \mathbf{T} at the solid–liquid interface can be determined. The tangential component of the stress acting in the liquid near the solid wall is expressed in terms of the unit vectors of the polar coordinate system as $\mathbf{e}_r \cdot \mathbf{T} \cdot \mathbf{e}_\theta$, which leads to the conclusion that shear-stress is determined by:

$$T_{r\theta} = -\frac{2\text{Ca}}{r} D \sin \hat{\theta} + O(1). \quad (2.74)$$

Thus, the shear-stress is proportional to r^{-1} , i.e., has exactly the singularity predicted by our simplified lubrication-type model. We note that pressure can be shown to have the same r^{-1} singularity [68].

2.2 Landau–Levich Problem

Moving contact lines discussed throughout most of the previous section are the so-called advancing contact lines: they advance into a region which is either dry or covered with a very thin precursor film. In many practical applications, the receding contact lines are also important, corresponding to the case when the moving interface leaves behind a region of the solid surface which is either dry or covered with a thin liquid film. The thickness of the latter is a function of the contact line speed and can be significantly higher than typical thickness values for the precursor films discussed in Sect. 2.1. The purpose of the present section is to discuss a model of the film left behind a moving interface using a simple configuration relevant for coating applications. A number of interesting phenomena observed when the solid surface behind a moving fluid interface is dry, i.e., the case of the “true” receding contact line, is beyond the scope of the present book but is discussed, e.g., in the review article of Bonn et al. [20].

Let us recall the static configuration of an air–liquid interface near a vertical solid wall discussed in Sect. 1.2 and sketched in Fig. 1.2. Now suppose that instead of being stationary the solid wall is moving upward at a speed U , as shown in Fig. 2.6, a situation relevant for dip coating and other similar practical applications. The problem of determining the interface shape for this geometric configuration, often referred to as the Landau–Levich problem, has been solved in [83]. The first step in the solution is developing a model of viscous flow in the liquid generated as a result of wall motion. Assuming steady flow at small values of the Reynolds number, we can use the Stokes flow equations, discussed in Sect. 1.5*. A nondimensional vector form of these equations is

$$\nabla p = \text{Ca} \nabla^2 \mathbf{u} + \mathbf{e}_g, \quad (2.75)$$

$$\nabla \cdot \mathbf{u} = 0. \quad (2.76)$$

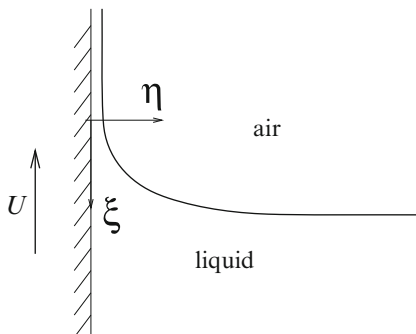


Fig. 2.6 Sketch of the geometry of the Landau–Levich problem

Here, \mathbf{e}_g is the unit vector in the direction of gravity, the components of the velocity vector \mathbf{u} are scaled by U , length variables by $a = \sqrt{\sigma/\rho g}$, and pressure by σ/a . The capillary number $\text{Ca} = \mu U/\sigma$ is typically small, suggesting that the mathematical description of the flow can be simplified further. The previously discussed lubrication-type models of thin films were based on the choices of scales which effectively made the left-hand side and the first term on the right-hand side of (2.75) equally important in the limit of $\text{Ca} \rightarrow 0$. Since the pressure gradients are determined by the capillary pressure jump at the interface, this mathematical formulation is equivalent to stating that viscous effects and surface tension both contribute to the shape of the interface. There is no reason to expect this to be the case everywhere in the configuration shown in Fig. 2.6. Far away from the slowly moving wall, the interface shape is not likely to be affected by the wall motion and is determined by the combined action of the capillary forces and gravity. The effects of viscosity and capillarity balance each other only near the wall, in a localized transition region of yet unknown characteristic dimensions L_ξ (along the wall) by L_η (normal to the wall). Let us describe the solution in this region using stationary Cartesian coordinates ξ and η shown in Fig. 2.6, scaled by L_ξ and L_η , respectively. The air-liquid interface is represented by a function $\eta = H(\xi)$ measuring the distance between the interface and the wall. Note that for sufficiently small slope of the interface, the capillary pressure jump is proportional to $H''(\xi)$ or, in dimensional terms, to $\sigma L_\eta/L_\xi^2$. Since the solution in the transition region and the static interface shape found in Sect. 1.2 have to be matched asymptotically in the limit of $\text{Ca} \rightarrow 0$, the characteristic capillary pressure jump in the transition region should be independent of the wall velocity. Therefore,

$$\frac{L_\eta}{L_\xi^2} \sim \text{const.} \quad \text{as} \quad \text{Ca} \rightarrow 0. \quad (2.77)$$

The capillary pressure gradient in the ξ -direction has to balance the effects of viscosity in the corresponding Stokes flow equation, which can now be written in nondimensional form as:

$$\frac{L_\eta}{L_\xi^3} p_\xi = \text{Ca} \left(\frac{1}{L_\xi^2} u_{\xi\xi} + \frac{1}{L_\eta^2} u_{\eta\eta} \right) + \frac{\rho g}{\sigma}. \quad (2.78)$$

Here, pressure is scaled by $\sigma L_\eta/L_\xi^2$, based on the estimate of the capillary pressure jump in the end of the previous paragraph, and the velocity u in the ξ -direction is scaled by U . Assuming that $L_\eta \ll L_\xi$, the capillary and viscous terms in (2.78) are of the same order when

$$\frac{L_\eta}{L_\xi} \sim \text{Ca}^{1/3}. \quad (2.79)$$

This condition together with (2.77) leads to

$$L_\xi \sim \text{Ca}^{1/3}, \quad L_\eta \sim \text{Ca}^{2/3}. \quad (2.80)$$

From now on, we *define* the scales L_ξ and L_η to be equal to $a\text{Ca}^{1/3}$ and $a\text{Ca}^{2/3}$, respectively. Using the same argument as in Sect. 1.4.2, we conclude that the ratio of the velocity scales in the two directions considered should be proportional to $\text{Ca}^{1/3}$, so the velocity component in the η -direction, v , is scaled by $\text{Ca}^{1/3}U$. By rewriting the standard dimensional Stokes flow equations from Sect. 1.5* in terms of our nondimensional variables and neglecting all terms which are small in the limit of $\text{Ca} \rightarrow 0$, we obtain

$$p_\xi = u_{\eta\eta}, \quad (2.81)$$

$$p_\eta = 0, \quad (2.82)$$

$$u_\xi + v_\eta = 0. \quad (2.83)$$

Applying similar nondimensionalization procedure to the standard dimensional boundary conditions formulated in Sect. 1.5* and taking the limit of $\text{Ca} \rightarrow 0$, we find

$$uH' - v = 0 \quad \text{at} \quad \eta = H(\xi), \quad (2.84)$$

$$u_\eta = 0 \quad \text{at} \quad \eta = H(\xi), \quad (2.85)$$

$$p = -H'' \quad \text{at} \quad \eta = H(\xi). \quad (2.86)$$

Here, we assume that the interface is stationary (defined by the function $H(\xi)$) and use primes to denote derivatives with respect to ξ . If there is no slip at the moving solid wall, the nondimensional boundary conditions there are written in the form

$$u = -1 \quad \text{at} \quad \eta = 0, \quad (2.87)$$

$$v = 0 \quad \text{at} \quad \eta = 0. \quad (2.88)$$

Integrating (2.83) in η with the conditions (2.84) and (2.88) leads to the integral mass balance of the form

$$\frac{d}{d\xi} \int_0^H u d\eta = 0, \quad (2.89)$$

which simply states that the flow rate in each cross-section normal to the ξ -axis is the same. The velocity profile $u(\eta)$ found by integrating (2.81) with the conditions (2.85) and (2.87) is

$$u = \frac{1}{2}p_\xi(\eta^2 - 2\eta H) - 1. \quad (2.90)$$

Substitution of this profile into (2.89) with subsequent integration in η leads to a differential equation for $H(\xi)$:

$$\left(\frac{H^3}{3} H''' - H \right)' = 0. \quad (2.91)$$

Integrating both sides in ξ and rearranging terms gives

$$H''' = \frac{3(H-b)}{H^3}. \quad (2.92)$$

Here, we introduced a constant b . Since the film is nearly flat for $\xi \rightarrow -\infty$, the constant b defines the scaled thickness of the film there and the following boundary conditions can be applied,

$$H(-\infty) = b, \quad H'(-\infty) = H''(-\infty) = 0. \quad (2.93)$$

Since b is unknown, an additional boundary condition is needed to determine the interface shape. It is obtained from the condition of matching to the local curvature of the static interface shape found in Sect. 1.2. According to (1.8), the dimensional curvature of the interface is equal to $\rho gh/\sigma$. Near the wall, the static solution reaches its maximum height determined by (1.10) and equal to $a\sqrt{2}$ for the case of perfect wetting. Thus, the dimensional curvature near the wall is $\sqrt{2}/a$, which in nondimensional terms gives the following matching condition

$$H''(\infty) = \sqrt{2}. \quad (2.94)$$

This completes our formulation of the boundary value problem for $H(\xi)$. However, developing a numerical solution procedure becomes more straightforward if (2.92) is written in the form independent from the unknown constant b using new variables

$$\hat{H} = \frac{H}{b}, \quad \hat{\xi} = \frac{3^{1/3}\xi}{b}. \quad (2.95)$$

In terms of these new variables, the interface shape is described by:

$$\hat{H}''' = \frac{\hat{H} - 1}{\hat{H}^3}, \quad (2.96)$$

$$\hat{H}(-\infty) = 1, \quad \hat{H}'(-\infty) = \hat{H}''(-\infty) = 0, \quad \hat{H}''(\infty) = \frac{b\sqrt{2}}{3^{2/3}}, \quad (2.97)$$

where the primes now denote derivatives with respect to $\hat{\xi}$. Suppose the origin of coordinates is chosen such that the solution near $\hat{\xi} = 0$ is close to $\hat{H} = 1$ and can therefore be represented by:

$$\hat{H} = 1 + \zeta, \quad |\zeta| \ll 1. \quad (2.98)$$

By substituting this expression into (2.96) and linearizing in ζ , we obtain

$$\zeta''' = \zeta. \quad (2.99)$$

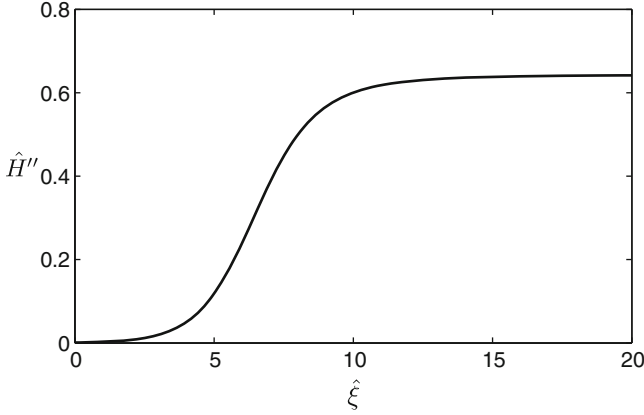


Fig. 2.7 Second derivative of the nondimensional interface position for the Landau–Levich problem, found by solving (2.96) with the conditions at $\hat{\xi} = 0$ given by (2.101), $\delta = 10^{-3}$

Solving this equation with the condition of $\zeta(-\infty) = 0$ leads to the formula

$$\zeta = \delta e^{\hat{\xi}}, \quad (2.100)$$

where δ is a constant. Based on (2.98), the values of the function \hat{H} and its derivatives at $\hat{\xi} = 0$ can then be expressed in terms of δ as follows,

$$\hat{H}(0) = 1 + \delta, \quad \hat{H}'(0) = \hat{H}''(0) = \delta. \quad (2.101)$$

Equation (2.96) is solved numerically with these conditions forward in $\hat{\xi}$ until $\hat{H}''(\hat{\xi})$ flattens out or, equivalently, $\hat{H}'''(\hat{\xi})$ approaches zero. We use $\delta = 10^{-3}$, although any small value can be chosen here since changing δ is equivalent to shifting the origin of coordinates (as long as $\delta \ll 1$). The MATLAB code for this problem can be found in Sect. B.3. Figure 2.7 illustrates the behavior of the second derivative of the interface shape obtained from the numerical solution, showing that at $\hat{\xi} \sim 10$ the derivative is already close to its asymptotic value, $\hat{H}''(\infty)$. Once the latter is obtained with the desired accuracy, the scaled trailing film thickness can be found based on $b = 3^{2/3} \hat{H}''(\infty) / \sqrt{2}$, resulting in the value of $b = 0.9458$. In dimensional terms, the final result for the thickness of the liquid film deposited on the wall can then be written as:

$$H^* = 0.9458 a \text{Ca}^{2/3}. \quad (2.102)$$

This result has been verified experimentally as discussed, e.g., in [88].

2.3 Axisymmetric Spreading of Thin Droplets

Both receding and advancing moving contact lines appear in a wide variety of applications. Understanding the behavior of dynamic contact angle as a function of local velocity is essential for correctly predicting the evolution of fluid interfaces seen in experiments. As a simple illustration, consider spreading of an axisymmetric droplet of a completely wetting liquid on a horizontal solid surface. The geometry of the problem is shown in Fig. 2.8. In the absence of evaporation and condensation, the droplet volume is constant during spreading, so it is convenient to take the cube root of the volume as the scale for all length variables. For small droplets, the Bond number (discussed in Sect. 1.2) is small, so we can neglect the effects of gravity. Since the changes in droplet shape are due to capillary forces only, this regime is often called “capillary spreading”. For relatively slow spreading considered here, one can assume that the droplet goes through a sequence of equilibrium shapes, which in the absence of gravity are the shapes of constant-curvature. For thin droplets, they are defined by:

$$h(r) = \frac{2}{\pi R^2} \left(1 - \frac{r^2}{R^2} \right), \quad (2.103)$$

where R is the scaled droplet radius, i.e., the distance from the axis of symmetry to the contact line, as shown in Fig. 2.8.

For each constant-curvature shape, the contact angle is nonzero, so none of these shapes represent a true equilibrium. The latter would require the contact angle to be equal to its static value, which for a completely wetting liquid considered here is zero. As discussed in Sect. 2.1, the apparent contact angle θ_{app} for a contact line moving at a speed U_{CL} can be approximated by:

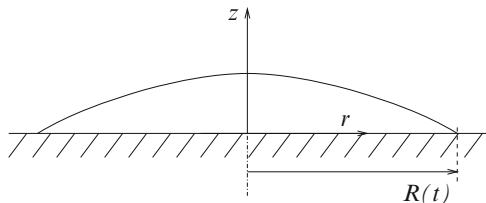
$$\theta_{\text{app}} \sim \left(\frac{\mu U_{\text{CL}}}{\sigma} \right)^{1/3}. \quad (2.104)$$

In our nondimensional variables, this implies

$$\theta_{\text{app}} \sim (R'(t))^{1/3}, \quad (2.105)$$

where the time scale is determined by the length scale divided by U_{CL} . Equation (2.103), on the other hand, allows us to approximate the apparent contact angle by

Fig. 2.8 Sketch of axisymmetric spreading droplet and cylindrical coordinates



the absolute value of $h'(r)$ at $r = R$, so that

$$\theta_{\text{app}} = \frac{4}{\pi R^3}. \quad (2.106)$$

By combining (2.105) and (2.106), we immediately obtain $R'(t) \sim R^{-9}$ and therefore

$$R(t) \sim t^{1/10}. \quad (2.107)$$

This power law has been indeed observed in several experiments, as discussed in more detail, e.g., in [20] and [97].

The solution above predicts that the droplet radius will grow indefinitely, although at a rapidly reducing rate. It may seem natural to assume that the spreading will continue until the continuum approximation breaks down, e.g., when droplet thickness is down to molecular dimensions. However, de Gennes [55] argued that the macroscopic model of spreading actually breaks down at much larger droplet thickness, when the effects of disjoining pressure (introduced in Sect. 1.7) become important and can result in an equilibrium pancake-type shape of the droplet. The thickness of such droplet is much larger than the molecular dimensions at which the continuum approximation breaks down.

It is important to emphasize that the power law given by (2.107) was derived based on the assumption of small Bond number, $\text{Bo} \ll 1$, so it breaks down when the Bond number is close to unity and the effects of gravity become comparable to those of surface tension. In the limit of $\text{Bo} \gg 1$, spreading is dominated by gravity rather than surface tension and a different power law for the radius $R(t)$ can be obtained, of the form

$$R(t) \sim t^{1/8}, \quad (2.108)$$

as discussed in detail, e.g., in Chap. 6 of Leal [87]. This result is obtained by considering the effects of gravity and viscous dissipation of energy in the bulk of the droplet. If most of the dissipation takes place near the contact line, the spreading law is in the form

$$R(t) \sim t^{1/7}.$$

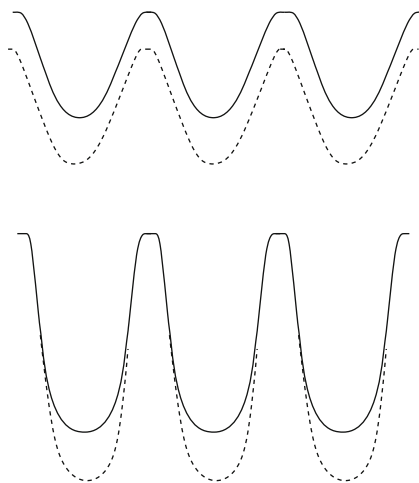
Comparison between different spreading laws and experimental data is discussed by Bonn et al. [20], Oron et al. [97], and Starov et al. [122].

2.4* Fingering Instability of Gravity-Driven Flow

2.4.1 Physical Phenomena

Gravity-driven flow of viscous liquid down an inclined plane can be described by two-dimensional models, such as the ones discussed in Sect. 2.1, only when the contact line remains straight as it moves down the incline. In experiments [69, 114],

Fig. 2.9 A sketch illustrating the shapes of deformed apparent contact line for patterns of wedge-shaped fingers (*top*) and rivulets (*bottom*) for flow down an incline. A view from the top is shown and liquid is above the contact line. Dashed lines show the contact line positions at a later moment in time. After [114]



even if the contact line is initially straight, it quickly deforms, resulting in the formation of finger-like structures. The instability leading to this pattern is referred to as *fingering instability* (although the same term is used for the instability of an interface moving in a narrow gap between two parallel plates or in a porous material [67]). Alternatively, the fingering instability of the gravity-driven flow has been referred to as the “rivulet instability.” Typical patterns seen in experiments on gravity-driven thin-film flow are illustrated by the sketches in Fig. 2.9. In Fig. 2.9 (top), the pattern consists of wedge-shaped fingers, while Fig. 2.9 (bottom) illustrates elongated fingers with nearly straight contact line on the sides; the latter are also often referred to as rivulets. Both patterns can be observed at the same inclination angle using different liquids. For example, Huppert [69] recorded wedge-shaped fingers for silicone oil and rivulets for glycerine for the inclination angle of $\alpha = 12^\circ$; note that the apparent contact angle was higher for glycerine. Similar fingering phenomena are observed in the process of spin coating in which the centrifugal force drives the flow of liquid over a solid surface. Formation of fingering pattern can result in poor quality of coating, so theoretical studies of fingering instability are important for practical applications in which spin coating process is used, e.g., in semiconductor industry.

The main mechanism of the instability has been elucidated by Spaïd and Homsy [119]. It can be explained as follows. Suppose, the contact line is a straight line moving downward at a constant velocity and the height of the capillary ridge is uniform along the direction of the contact line. Recall that the capillary ridge is a common feature of two-dimensional interface shapes, formed as a result of accumulation of liquid behind the apparent contact line, as seen, e.g., in Fig. 2.3. Suppose a small localized bump is formed on top of the capillary ridge as a result of random fluctuations. Then the viscous resistance to the flow in the bump region will be less due to increased local thickness of the film there and the bump will move downward faster than the parts of the capillary ridge away from it, leading to the fingering instability.

The above explanation of the instability mechanism is, of course, only qualitative. In order to develop a quantitative model of the phenomenon, it is natural to employ the ideas of lubrication-type approach since the film thickness is typically small compared to all other macroscopic length scales observed in the system. However, the evolution equation derived in Sect. 2.1 is not directly applicable to the present situation since the assumption of two-dimensionality (film thickness being a function of time and the x -variable) is no longer applicable. Therefore, our first step is to generalize the lubrication-type approach used in Sect. 2.1 to a situation when the liquid–gas interface is a two-dimensional surface and the liquid flow is three-dimensional.

2.4.2 Lubrication-Type Equations in 3D

The key steps in the derivation presented in this subsection are essentially the same for a wide range of problems including fingering instability, nonaxisymmetric spreading of thin liquid droplets, and growth of dry patches in thin liquid films. These steps are illustrated here in the context of fingering instability for gravity-driven flow down a flat solid plate inclined at an angle α . The film far upstream from the contact line is assumed flat and of thickness d , so the characteristic flow velocity U and the capillary number Ca are still defined by (2.1) and (2.2). The formulation is very similar to the one used in the first section of this chapter except that we no longer invoke the assumption of two-dimensional flow and use a different notation for the scaled Cartesian coordinates: the z -coordinate measures the distance in the direction normal to the plate, scaled by d , while the xy plane coincides with the solid surface. Both x and y are scaled by $d/Ca^{1/3}$, and the x -axis is in the direction of fastest descent along the inclined surface. The lubrication-type equations for the flow are

$$p_x = u_{zz} + 1, \quad (2.109)$$

$$p_y = v_{zz}, \quad (2.110)$$

$$p_z = 0, \quad (2.111)$$

$$u_x + v_y + w_z = 0. \quad (2.112)$$

Here u and v are velocities in the x - and y -directions, respectively, both scaled by U . The velocity in the z -direction, w , is scaled by $Ca^{1/3}U$, and the pressure p is scaled by $Ca^{2/3}\sigma/d$.

At the two-dimensional interface, defined by the function $z = h(x, y, t)$, we use the nondimensional versions of the general interfacial conditions formulated in Sect. 1.5*. In the limit of small capillary numbers, these nondimensional conditions simplify to

$$h_t + uh_x + vh_y - w = 0 \quad \text{at} \quad z = h(x, y, t), \quad (2.113)$$

$$u_z = 0 \quad \text{at} \quad z = h(x, y, t), \quad (2.114)$$

$$v_z = 0 \quad \text{at} \quad z = h(x, y, t), \quad (2.115)$$

$$p = -\nabla^2 h \quad \text{at} \quad z = h(x, y, t), \quad (2.116)$$

where we use the operator $\nabla = (\partial/\partial x, \partial/\partial y)$ and the time variable scaled by $\text{Ca}^{-1/3}d/U$.

At the solid boundary, the no-slip condition is satisfied and the normal velocity is zero, so

$$u = v = w = 0 \quad \text{at} \quad y = 0. \quad (2.117)$$

By repeating the same steps as in the derivation of (2.14), the following evolution equation is obtained

$$h_t + \frac{1}{3} \nabla \cdot (h^3 \nabla^2 h) + h^2 h_x = 0. \quad (2.118)$$

As with the two-dimensional version of this problem discussed in Sect. 2.1, it is convenient to introduce a moving reference frame by defining

$$\hat{x} = x - u_{\text{CL}} t, \quad u_{\text{CL}} = \frac{1}{3}(1 + b + b^2), \quad (2.119)$$

where b is the scaled thickness of the precursor film, introduced in Sect. 2.1.3. In the moving reference frame, (2.118) can be written as:

$$h_t - \frac{1}{3}(1 + b + b^2)h_{\hat{x}} + \frac{1}{3} \hat{\nabla} \cdot (h^3 \hat{\nabla}^2 h) + h^2 h_{\hat{x}} = 0, \quad (2.120)$$

where $\hat{\nabla} = (\partial/\partial \hat{x}, \partial/\partial y)$. Far upstream and downstream from the apparent contact line the film is assumed to be flat, with the local thickness values specified as:

$$h(-\infty, y, t) = 1, \quad h(\infty, y, t) = b. \quad (2.121)$$

2.4.3 Linear Stability

Equation (2.120) has a two-dimensional steady-state solution $h = h_0(\hat{x})$ found in Sect. 2.1. However, in order for this solution to be observed in experiments, it has to be stable with respect to small perturbations. Stability conditions can be obtained using the linear stability theory. Let us introduce a small perturbation of the steady-state solution,

$$h(\hat{x}, y, t) = h_0(\hat{x}) + \zeta(\hat{x}, y, t), \quad |\zeta| \ll |h_0|. \quad (2.122)$$

Substituting this form of the solution into (2.120) and neglecting terms which are nonlinear in the small perturbation ζ , we obtain a linearized equation for the perturbation:

$$\zeta_t - \frac{1}{3}(1 + b + b^2)\zeta_{\hat{x}} + \frac{1}{3} \hat{\nabla} \cdot (h_0^3 \hat{\nabla}^2 \zeta) + (h_0^2 h_0'''\zeta)_{\hat{x}} + h_0^2 \zeta_{\hat{x}} + 2h_0 h_0' \zeta = 0, \quad (2.123)$$

where primes are used to denote derivatives with respect to \hat{x} . Due to linearity of the equation for ζ , any perturbation which is periodic in the y -direction can be represented as a superposition of perturbations of the form

$$\zeta = G(\hat{x})e^{\gamma t +iky}, \quad (2.124)$$

where γ and k denote the growth rate and the wavenumber of the perturbation, respectively, both expressed in nondimensional terms; $G(\hat{x})$ is a function to be determined as part of the solution. Note that ζ is not periodic in the \hat{x} -direction due to the conditions of flat film far upstream and downstream from the apparent contact line, so the function $G(\hat{x})$ cannot be represented as a superposition of sinusoidal perturbations in the \hat{x} -direction. The stability problem is now reduced to finding an expression for the perturbation growth rate γ as a function of its wavenumber k . Since the extent of the domain in both positive and negative y -directions is infinite, perturbations of all wavenumbers should be considered in the analysis. By substituting the form of the perturbation (2.124) into (2.123), we obtain

$$\gamma G - \frac{1}{3}(1+b+b^2)G' + \left[\frac{h_0^3}{3}(G''' - k^2 G') + h_0^2(h_0''' + 1)G \right]' + \frac{h_0^3}{3}(k^4 G - k^2 G'') = 0. \quad (2.125)$$

The perturbation does not affect the solution far upstream from the apparent contact line or in the precursor film, so the function $G(\hat{x})$ satisfies the conditions

$$G(-\infty) = G'(-\infty) = G(\infty) = G'(\infty) = 0. \quad (2.126)$$

Equations (2.125) and (2.126) define an *eigenvalue problem*, meaning that the nontrivial solutions exist only for certain values of γ . To solve this eigenvalue problem numerically, we consider (2.125) on a finite domain $[0, L]$, assuming that G is zero outside of this domain and satisfies

$$G(0) = G'(0) = G(L) = G'(L) = 0. \quad (2.127)$$

We discretize the domain $[0, L]$ using a uniform mesh and apply the standard finite difference formulas for the derivatives of G . The function h_0 and its derivatives are evaluated based on the numerical solutions obtained in Sect. 2.1 using the code from Sect. B.2.1 and illustrated in Fig. 2.3. The discretized version of the problem then takes the form

$$\gamma \mathbf{G} = \mathbf{A} \mathbf{G}, \quad (2.128)$$

where \mathbf{A} is a known matrix which depends on h_0 and the mesh size, \mathbf{G} is the vector of values of the function G at the mesh points. The system can now be solved using standard numerical methods for finding eigenvalues of matrices, e.g., in MATLAB. The value of γ with the largest real part determines stability and is shown as a function of the wavenumber in Fig. 2.10 for different values of the precursor film thickness. Based on the numerical solution, the system is always unstable.

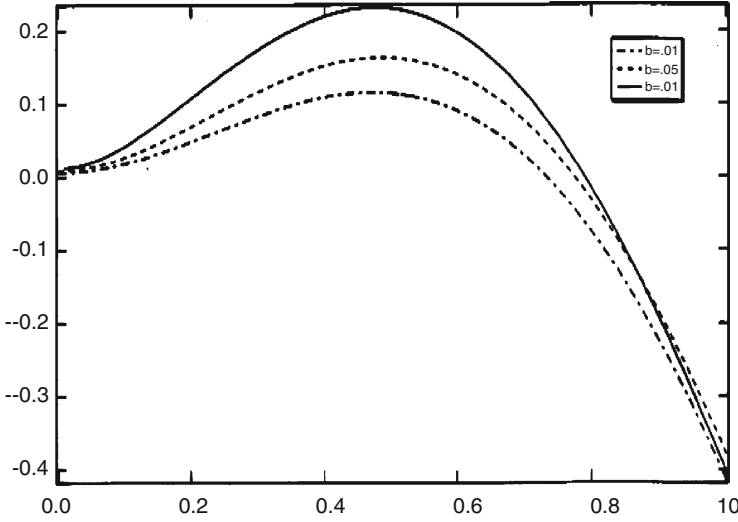


Fig. 2.10 A plot of perturbation growth rate versus the wavenumber based on the numerical solution of (2.125). From [119], reprinted with permission of AIP

A simple plot of different terms in the expression for γ shows that the terms corresponding to gravity effect (and not various terms corresponding to surface tension effects) are most important for the instability, thus justifying the explanation of the instability mechanism discussed in the beginning of this section. This argument can be made more rigorous by considering the rate of energy dissipation as was done by Spaid and Homsy [119].

2.4.4 Numerical Simulations

The linear stability analysis only describes evolution of small perturbations of the two-dimensional solution, so it is not applicable to modeling the interface shapes seen, e.g., in Fig. 2.9. In order to describe experimentally observed fingering patterns, (2.120) has to be solved numerically. For the numerical simulations, a finite size domain has to be chosen. We consider (2.120) on a rectangular domain

$$0 \leq \hat{x} \leq L, \quad 0 < y < \tilde{L}. \quad (2.129)$$

and use the boundary conditions

$$h(0, y, t) = 1, \quad h(L, y, t) = b \quad (2.130)$$

together with the no-flux conditions as described in [80]. Since the experimental fingering patterns such as the ones seen in Fig. 2.9 are usually nearly periodic, we use the periodic boundary conditions at $y = 0$ and $y = \tilde{L}$.

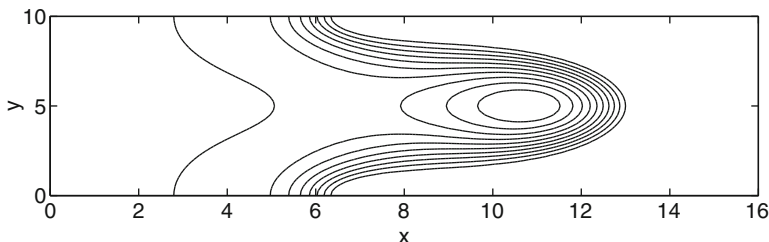


Fig. 2.11 A wedge-shaped finger obtained from numerical simulation of fingering instability for the case of perfect wetting

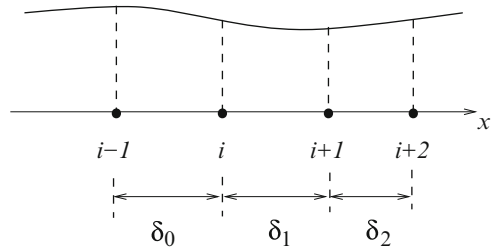
Different approaches have been used for numerical simulations of fingering. Many of them are based on ADI (alternating direction implicit), an efficient method which allows one to track evolution of two-dimensional interfaces without having to deal with very large matrices [140]. However, recent progress in matrix computations suggests that even a more straightforward method, a version of the method of lines with iterative approaches to matrix inversion is suitable for numerical studies of fingering. Mesh refinement near the contact line, where the interface slope changes most rapidly, makes the simulations more efficient; evaluation of derivatives in this framework is discussed in the following subsection. Numerical simulations have been conducted for both precursor model [51, 80] and the Navier–Greenspan slip model [94], and are in agreement with the linear stability results when the deviation of the interface shape from the solution described by $h_o(\hat{x})$ is small. Some issues have been raised regarding the validity of the linear theory at small inclination angles, and are attributed to the non-self-adjoint nature of the linear operator involved, as discussed by Bertozzi and Brenner [148] and Grigoriev [60].

Numerical simulations of strongly nonlinear evolution of the interface (outside the range of validity of the linear theory) allowed several groups [51, 80, 94] to obtain two different shapes of fingers found in experiments (and shown in Fig. 2.9) and identify criteria for the transition between them. Here, the discussion is based on the work of Moyle et al. [94], in which the contact angle θ is a parameter of the problem and the Navier–Greenspan condition is used to eliminate the shear-stress singularity. For the values of θ equal or close to zero, the pattern is that of wedge-shaped fingers and is steady in a moving reference frame. An example of a wedge-shaped finger seen in numerical simulations is shown in Fig. 2.11 and can be compared to the sketch in Fig. 2.9(top). As the contact angle is increased, fingers become more elongated and eventually transition to rivulet-type shapes. From a practical point of view, it is most important to identify the transition to straight-sided rivulets such that the front of the pattern advances but the troughs between the rivulets remain stationary. This type of pattern results in failure to completely coat the solid surface with a layer of liquid. Complete coating is usually the goal in practical applications. Moyle et al. [94] observe that in the numerical simulation the transition takes place at

$$(\mu U / \sigma)^{-1/3} \tan \theta \approx 1, \quad (2.131)$$

where U is defined by (2.1).

Fig. 2.12 Sketch of a nonuniform mesh in the vicinity of a mesh point i



2.4.5 Finite-Difference Method with Nonuniform Mesh

In order to develop efficient numerical methods for problems in which the derivatives of the interface shape become large in localized regions in space, one has to consider using nonuniform meshes. The goal of the present section is to provide brief derivations of the basic finite-difference formulas for derivatives on nonuniform meshes.

Consider an arbitrary nonuniform mesh as sketched in Fig. 2.12. We assume that as the mesh is refined, the distances between mesh points change according to $\delta_k = A_k \delta$, where the constants A_k do not change. As a simple illustration of the method, let us evaluate the second derivative of the interface at the mesh point i in terms of values of h at points in its vicinity. Using Taylor series,

$$h_{i+1} = h_i + h' \delta_1 + \frac{1}{2} h'' \delta_1^2 + O(\delta^3), \quad (2.132)$$

$$h_{i-1} = h_i - h' \delta_0 + \frac{1}{2} h'' \delta_0^2 + O(\delta^3), \quad (2.133)$$

where h' and h'' are the (unknown) exact values of the derivatives at the point i . The notation $O(\delta^3)$ refers to behavior in the limit of $\delta \rightarrow 0$, which is appropriate to consider since δ becomes small as the mesh is refined.

Dividing (2.132) by δ_1 , (2.133) by δ_0 , and adding the two together allows us to eliminate h' . Then, h'' is expressed as:

$$h'' = \frac{2}{\delta_0 + \delta_1} \left(\frac{h_{i+1} - h_i}{\delta_1} + \frac{h_{i-1} - h_i}{\delta_0} \right) + O(\delta). \quad (2.134)$$

The same approach can be used to express higher-order derivatives except that more mesh points are needed.

Derivatives at points halfway between the mesh points are also often needed for numerical schemes. Let us derive a formula for the third derivative of the interface shape at $i + \frac{1}{2}$ (half-way between the points i and $i + 1$). Taylor series can be used to express h_{i+1} in terms of the values of the function h and its derivatives (h' , h'' , and h''') at $i + \frac{1}{2}$ as follows,

$$h_{i+1} = h + h' \frac{\delta_1}{2} + h'' \frac{\delta_1^2}{8} + h''' \frac{\delta_1^3}{48} + O(\delta^4). \quad (2.135)$$

Similar expansions can be written for h_i , h_{i+2} , and h_{i-1} . When the $O(\delta^4)$ terms in all these expansions are neglected, a linear 4×4 system of equations is obtained. By solving this system, we express the third derivative at $i + \frac{1}{2}$ in term of function values at mesh points,

$$h''' = \frac{6}{S_\delta} \left[\frac{h_{i+2}}{\delta_2(\delta_1 + \delta_2)} - \frac{h_{i+1}S_\delta}{\delta_1\delta_2(\delta_0 + \delta_1)} + \frac{h_iS_\delta}{\delta_0\delta_1(\delta_1 + \delta_2)} - \frac{h_{i-1}}{\delta_0(\delta_0 + \delta_1)} \right]. \quad (2.136)$$

Here, $S_\delta = \delta_0 + \delta_1 + \delta_2$. The formula above and a similar expression for the third derivative at $i - 1/2$ have been used in the numerical simulations of fingering instability.

2.5 Notes on Literature

Several well-known reviews address the issue of contact line singularity and approaches to resolving it [20, 55, 70]. The Landau–Levich problem is discussed in detail in the classical book of Levich [88]. Literature on the fingering instability of gravity-driven flow is reviewed by, e.g., Oron et al. [97] and Craster and Matar [40].

Interfacial Fluid Mechanics
A Mathematical Modeling Approach

Ajaev, V.S.

2012, X, 214 p., Hardcover

ISBN: 978-1-4614-1340-0